Engineering xxx (xxxx) xxx

Contents lists available at ScienceDirect

Engineering

journal homepage: www.elsevier.com/locate/eng

Research
Environmental Engineering—Article

Mass Transfer-Promoted Fe^{2+}/Fe^{3+} Circulation Steered by 3D Flow-Through Co-Catalyst System Toward Sustainable Advanced Oxidation Processes

Weiyang Lv [a,b,*], Hao Li [a], Jinhui Wang [a], Lixin Wang [a], Zenglong Wu [a], Yuge Wang [a], Wenkai Song [a], Wenkai Cheng [c,*], Yuyuan Yao [a,b]

[a] National Engineering Lab of Textile Fiber Materials and Processing Technology (Zhejiang), Zhejiang Sci-Tech University, Hangzhou 310018, China
[b] Zhejiang Provincial Innovation Center of Advanced Textile Technology, Shaoxing 312000, China
[c] Jiangsu Ruiya Stirring Technology Co., Ltd., Yixing 214200, China

ARTICLE INFO

Article history:
Available online xxxx

Keywords:
Advanced oxidation processes
3D co-catalyst
Flow-through mode
Enhanced mass transfer
Complex wastewater treatment

ABSTRACT

Realizing fast and continuous generation of reactive oxygen species (ROSs) via iron-based advanced oxidation processes (AOPs) is significant in the environmental and biological fields. However, current AOPs assisted by co-catalysts still suffer from the poor mass/electron transfer and non-durable promotion effect, giving rise to the sluggish Fe^{2+}/Fe^{3+} cycle and low dynamic concentration of Fe^{2+} for ROS production. Herein, we present a three-dimensional (3D) macroscale co-catalyst functionalized with MoS_2 to achieve ultra-efficient Fe^{2+} regeneration (equilibrium Fe^{2+} ratio of 82.4%) and remarkable stability (more than 20 cycles) via a circulating flow-through process. Unlike the conventional batch-type reactor, experiments and computational fluid dynamics simulations demonstrate that the optimal utilization of the 3D active area under the flow-through mode, initiated by the convection-enhanced mass/charge transfer for Fe^{2+} reduction and then strengthened by MoS_2-induced flow rotation for sufficient reactant mixing, is crucial for oxidant activation and subsequent ROS generation. Strikingly, the flow-through co-catalytic system with superwetting capabilities can even tackle the intricate oily wastewater stabilized by different surfactants without the loss of pollutant degradation efficiency. Our findings highlight an innovative co-catalyst system design to expand the applicability of AOPs based technology, especially in large-scale complex wastewater treatment.

1. Introduction

The generation of highly reactive oxygen species (ROSs) has played a critical role in the environmental and biomedical fields over the past few decades [1,2]. Among the various approaches for ROS production, advanced oxidation processes (AOPs), especially the peroxymonosulfate (PMS) based AOPs, have received considerable attention because the PMS can serve as the ideal reservoir for the controllable production of multiple ROS, such as sulfate radical ($SO_4^{\cdot-}$), hydroxyl radical ($^{\cdot}OH$), superoxide radical ($O_2^{\cdot-}$), and singlet oxygen ($^1O_2$) [3–5]. Consequently, the PMS-triggered AOPs can be applied in diverse domains, including organic synthesis, cancer therapy and wastewater remediation [6–8]. As the benchmark catalyst in the classical Fenton reaction, Fe^{2+} has also been used for PMS activation owing to its environment-benignancy, cost effectiveness and high reactivity, which can boost the heterolytic cleavage of PMS through single-electron transfer process [9,10]. Nevertheless, the application potential of the Fe^{2+}/PMS system remains challenging in view of the low efficiency of PMS decomposition and undesirable precipitation of iron hydroxide sludge, mainly resulting from the sluggish conversion of Fe^{3+} back to Fe^{2+} during reaction [11,12]. To overcome the intrinsic drawbacks, breakthroughs in accelerating the Fe^{3+}/Fe^{2+} redox cycles for the successive activation of PMS are urgently demanded.

In principle, the essence of Fe^{3+}/Fe^{2+} conversion is to accept additional electrons, and high-speed electron transfer poses a significant impact on Fe^{3+} reduction [13]. To date, various auxiliary methods have been adopted to expedite the regeneration rate of

* Corresponding authors.
E-mail addresses: wylv@zstu.edu.cn (W. Lv), chengwenk@163.com (W. Cheng).

https://doi.org/10.1016/j.eng.2023.06.010

Please cite this article as: W. Lv, H. Li, J. Wang et al., Mass Transfer-Promoted Fe^{2+}/Fe^{3+} Circulation Steered by 3D Flow-Through Co-Catalyst System Toward Sustainable Advanced Oxidation Processes, Engineering, https://doi.org/10.1016/j.eng.2023.06.010

Fe^{2+} by introducing external stimulations, such as ultraviolet–visible (UV/Vis) light, electricity, ultrasound, and chemical promotors [14–17]. Thereinto, directly adding the reductant as the "co-catalyst" can remarkably accelerate the Fe^{3+}/Fe^{2+} circulation with a relatively low cost and simple operation procedure, which is considered one of the most promising options for the actual application [18,19]. Until now, a variety of co-catalysts have been explored and can be mainly classified into organic reductive agents and inorganic heterogeneous compounds. The organic agents including ascorbic acid, hydroxylamine, and protocatechuic acid can provide a homogenous reaction environment for the rapid reduction of Fe^{3+} [20–22], thus facilitating the direct reaction between Fe^{2+} and PMS. However, the organic co-catalysts can be easily consumed by the generated ROS, making it very difficult to achieve the long-term promotion effect. More recently, inorganic heterogeneous co-catalysts such as metal sulfides, metal oxides, and nonmetallic elements (boron, carbon, and phosphorus) with strong electron-donating ability have been used to improve the overall efficiency of AOPs [23–28]. Although the inorganic co-catalysts exhibit higher chemical stability than organic agents, two fundamental challenges still need to be addressed to further promote the capability of co-catalyst system in treating practical wastewater: ① the reported inorganic co-catalysts are commonly in the powder state, revealing that they are difficult to be collected, which will inevitably deteriorate the reusability and increase the operational cost [29]. Further, loading the co-catalysts on the porous substrate can alleviate the issue to some degree [30], while a new concern regarding the mass transfer limitation may arise due to the insufficient contact between the reactants and the interior part of the co-catalyst composite, resulting in their ineffectiveness in treating large-scale wastewater; and ② most industrial wastewater is intricate with multiple contaminants, containing not only organic pollutants but also insoluble oily compounds [31]. The oil droplets might attach to the co-catalyst surface and pose an adverse impact on the mass transfer of Fe species in the co-catalytic system, thus slowing down the Fe^{3+}/Fe^{2+} circulation, yet few attempts have paid attention to this intractable problem. Under these circumstances, it is of both scientific significance and practical value to construct a novel co-catalyst system that can maintain remarkable reusability and minimize the mass transfer limitation in industrial wastewater treatment.

Herein, we conceive a flow-through co-catalyst system that successfully addresses the two aforementioned bottlenecks of current AOPs. This system is established by two key innovations: first, a three-dimensional (3D) multifunctional material was constructed through the *in situ* growth of molybdenum disulfide (MoS_2) on the commercial activated carbon fibers (ACFs), where the synthesized MoS_2 could endow the ultimate ACFs with superwetting property and synergistic co-catalytic capability. Meanwhile, the loading of MoS_2 on the ACFs could bypass the redundancy of co-catalyst recovery. Second, a flow-through wastewater treatment system was designed by combining the 3D co-catalyst and peristaltic pump, which could efficiently separate the oil droplets and enable optimal utilization of catalytic sites inside the 3D porous material through forced convection, thereby avoiding the interference of oil droplets and guaranteeing the enhanced mass transfer for efficient AOPs. Both detailed experimental results and computational fluid dynamics (CFDs) simulations confirmed the significant improvement of mass transfer in the flow-through catalytic system, giving rise to the higher Fe^{2+} regeneration (equilibrium Fe^{2+} ratio of 82.4%) and PMS decomposition efficiency (over 96.1%). More excitingly, the 3D co-catalyst system exhibited superior performance and higher stability than other popular metal sulfides, metal oxides and nonmetallic materials when treating the large amount of wastewater, and could even tackle the intricate oily wastewater without the loss of degradation efficiency. This study offers an effective strategy to rationally design co-catalyst system for AOPs and other related chemical processes.

2. Experimental section

2.1. Chemicals and materials

ACFs were purchased from Jiangsu Sutong Carbon Fiber Co., Ltd. (China). Dopamine hydrochloride ($C_8H_{11}NO_2{\cdot}HCl$), potassium monopersulfate triple salt ($2KHSO_5{\cdot}KHSO_4{\cdot}K_2SO_4$), thioacetamide ($C_2H_5NS$), bisphenol A (BPA), methanol (MA), benzoquinone (P-BQ), tris(hydroxymethyl)aminomethane (Tris), zinc sulfide (ZnS; 99.99%), tungsten sulfide (WS_2; 99.9%, 25 μm), ferrous sulfide (FeS; Fe: 60.0%–72.0%), boron nitride (BN; 99.9%, 1–2 μm), stannic oxide (SnO_2; analytical reagent (analytical reagent (AR), 99.5%), cobaltosic oxide (Co_3O_4; 99.0%), zinc oxide (ZnO; 99.99%), cupric oxide (CuO; AR, 99%), and L-histidine (L-His) were purchased from Aladdin Co., Ltd. (China). Red phosphorus (RP; 98.5%, grain size: 150 μm) was purchased from Energy Chemical Co., Ltd. Graphite nanosheet (GNP; 99%, grain size: 150 μm) was purchased from Hanhui Graphite Co., Ltd. Ammonium molybdate ($(NH_4)_2MoO_4$) and 5,5-dimethyl-pyrroline-N-oxide (DMPO) were supplied by Macklin Co., Ltd. (China). 2,2,6,6-tetramethyl-4-piperidinone (TEMP) was purchased from J&K Scientific Co., Ltd. All other reagents were provided by Mike Chemical Instrument Co., Ltd. (China). C_3N_4 was obtained by calcining urea at 550 °C for 3 h. Deionized (DI) water was used throughout the experiments. All reagents were used as received without further purification.

2.2. Synthesis of ACFs–polydopamine

Firstly, the ACFs were soaked in the sufficient amount of nitric acid solution (3 $mol{\cdot}L^{-1}$) for pretreatment, and then the treated ACFs were fully washed and dried for later use. Subsequently, an appropriate amount of dopamine hydrochloride was added to the tris solution (100 mL) with continuous stirring until completely dissolved. Thereafter, the treated ACFs (2.5 cm × 2.5 cm) were immersed into the above mixed solution and oscillated at 25 °C for 12 h. Finally, the modified ACFs were rinsed and dried, and then named ACFs–polydopamine (PDA), abbreviated as AP.

2.3. Synthesis of ACFs–PDA–MoS_2

An appropriate amount of $(NH_4)_2MoO_4$ and C_2H_5NS were added to DI water (50 mL) and fully dissolved by ultrasonication. Subsequently, AP was immersed into the above reaction solution and the mixture was then transferred to a 100 mL autoclave for hydrothermal reaction at 200 °C for 18 h. Finally, the modified sample with MoS_2 on the surface was obtained (ACFs–PDA–MoS_2), named APM. For comparison, MoS_2 particles were synthesized under the same reaction conditions, and the sample of MoS_2 directly grown on the pristine ACFs surface (ACFs–MoS_2) was abbreviated as AM.

2.4. Reaction procedure

Batch-type catalytic reaction: The removal experiments were carried out in a 100 mL conical flask with the temperature of 25 °C. The reaction volume of 50 mL was used in all the experiments and the specific reaction conditions were as follows: pollutants (50×10^{-6} $mol{\cdot}L^{-1}$, 50 mL); catalysts (0.5 $g{\cdot}L^{-1}$); Fe^{2+} (0.04×10^{-3} $mol{\cdot}L^{-1}$); and PMS (1×10^{-3} $mol{\cdot}L^{-1}$). In a shaker at 150 revolutions per minute (rpm), 1.5 mL of the mixed reaction solution was extracted at a given interval (2 min) and filtered through a 0.45 μm Millipore filter, followed by a test with

UV–vis spectrophotometer and high performance liquid chromatography (HPLC). In batch-type catalytic degradation experiments, the removal rates of pollutants were calculated by $(1 - C/C_0) \times 100\%$ (C and C_0 represented the residual and initial concentration of the pollutants). The degradation of all pollutants followed the pseudo-first-order kinetics: $\ln(C/C_0) = -K_{obs}t$, where K_{obs} and t represented the apparent rate constant and reaction time.

Flow-through catalytic reaction: The removal experiments were carried out in a 200 mL conical flask with the temperature of 25 °C. The reaction volume of 100 mL was used in the removal experiments and the specific reaction conditions were as follows: pollutants (50×10^{-6} mol·L^{-1}, 100 mL); catalysts (0.25 g); Fe^{2+} (0.04×10^{-3} mol·L^{-1}); PMS (1×10^{-3} mol·L^{-1}). In a peristaltic pump flow rate of 200 mL·min^{-1}, 1.5 mL of the mixed reaction solution was extracted at a given interval (2 min) and filtered through a 0.45 μm Millipore filter, followed by a test with UV–vis spectrophotometer and HPLC.

Oil-in-water emulsion separation: The oil-in-water emulsion was prepared by adding *n*-hexane (1.5 mL) into DI water (148.5 mL) with Tween-80 (1.5 mg) as the surfactant, and then mixed by the homogenizer (T25, IKA, Germany) at a speed of 5000 rpm for 10 min. The separation process of oil-in-water emulsion was carried out via a home-made filtration unit where the modified samples were sandwiched between two silica gaskets. The prepared emulsion could go through the samples by gravity. In oil-in-water emulsion separation experiments, the oil rejection was recorded according to the oil contents in feed and in corresponding filtrate with the UV–vis spectrophotometer (the oil was dyed with red O), the oil rejection rates were evaluated by $(1 - C_{oil}/C_{0,oil}) \times 100\%$, where C_{oil} and $C_{0,oil}$ were the oil content in the filtrate and the feed emulsion, respectively.

2.5. Characterizations

The morphology of the as-prepared materials was characterized by a scanning electron microscopy (SEM; Ultra-55, Zeiss, Germany). Transmission electronic microscopy images were obtained on a transmission electron microscopy (TEM; JEOL JEM 2100, 200 kV). The crystal structure and phase of modified ACFs were examined by an X-ray diffraction (XRD; Bruker D8, Germany). The chemical bonds of the modified materials were characterized by a Fourier-transform infrared (FT-IR; ThermoFisher, USA) spectroscopy. The surface elements and valence state of modified materials were investigated by X-ray photoelectron spectroscopy (XPS; Thermo Scientific K-Alpha, USA). The electron paramagnetic resonance spectra were recorded via a Bruker A300 spectrometer. The contact angle was measured via a contact angle measurement instrument (JCY, Shanghai FangRui Instrument Co., Ltd., China).

2.6. CFDs simulation

CFDs simulation was performed by using the commercial ANSYS Fluent 15.0 software (ANSYS Inc., USA). The laminar water flow in these microchannels was assumed to be isothermal and incompressible. No-slip boundary condition was imposed on the wall and surface of fiber, which was assumed to be impermeable. The velocity-inlet boundary was imposed on the inlet and the pressure-out boundary was imposed on the outlet. The velocity magnitude of inlet was 0.5 m·s^{-1}. Two flow modes were simulated.

3. Results and discussion

3.1. Synthesis and characterization of 3D co-catalyst APM

Fig. 1(a) elucidated the facile synthesis of APM through the *in situ* growth of MoS_2 on the PDA modified nanofibrous mats by a hydrothermal reaction. In this study, commercially available ACFs constructed by the 3D interlaced carbon fibers were ingeniously selected as the substrate due to its robustness, chemical stability and high porosity (Fig. S1). After the successful deposition of the PDA layer on the ACFs surface, the pristine smooth fibers became coarser without changing the original network (denoted as AP, Fig. S2). Subsequently, the immense growth of flower globose-like MoS_2 particles on the carbon fiber was achieved with progress in the hydrothermal reaction (Figs. 1(b) and (c)). The corresponding element mapping in Fig. 1(d) revealed the uniform distribution of S and Mo elements on the APM surface, indicating the successful synthesis of MoS_2 on the substrate, which was also supported by the XRD and FT-IR results (Figs. S3 and S4) [32]. By contrast, the control sample fabricated via the identical synthesis procedure except for the PDA modification (denoted as AM) displayed the markedly different morphology, where the tiny MoS_2 nanosheets grew vertically on the fiber and formed a thin mineral coating on the fiber surface (Fig. S5). This distinct result suggested that the PDA intermediate layer on the fiber surface was beneficial to the full growth of MoS_2, mainly resulting from the multifunctional groups of PDA for metal complexation [33], which could help anchor MoS_2 on ACFs and also prevent it from falling off.

High-resolution transmission electron microscopy (HRTEM) analysis was then employed to reveal the morphology and structure of MoS_2 on the APM surface. The image in Fig. 1(e) suggested the co-existence of hexagonal 2H phase and trigonal 1 T phase in MoS_2 particles. The chemical feature of MoS_2 was corroborated by Raman spectrum (Fig. S6), where two peaks at 380 and 408 cm^{-1} corresponding to the in-plane E^1_{2g} and out-of-plane A_{1g} lattice vibrations of 2H phase MoS_2 were observed. Meanwhile, the characteristic peaks centered at 152, 226, and 325 cm^{-1} could be attributed to J_1, J_2, and J_3 modes of 1 T phase MoS_2, respectively [34]. The XPS also manifested the mixed phase structure of MoS_2 in APM (Figs. S7 and S8). In the Mo 3d spectrum, the binding energies at 229.3 and 232.6 eV (1 eV = 1.602176×10^{-19} J) were attributed to the Mo $3d_{5/2}$ and Mo $3d_{3/2}$ of 2H phase MoS_2, accompanied by the typical peaks of 1 T phase MoS_2 at 228.9 and 232.1 eV (Fig. 1(f)) [35]. The above analysis confirmed that MoS_2 particles were successfully grown on the APM surface with the mixed composition of 2H and 1 T phases.

In addition, the microstructure of the prepared ACFs, AP, and APM was determined by N_2 adsorption–desorption isothermal method. These samples all showed similar isotherm types belonging to I-type isotherm curves, suggesting that the surface of ACFs, AP, and APM possessed a typical porous structure (Fig. S9). Specifically, the Brunauer–Emmett–Teller surface areas of ACFs, AP, and APM were calculated to be 937.1, 110.0, and 602.0 m^2·g^{-1}, and the pore volumes of these samples were 0.40, 0.07, and 0.26 cm^3·g^{-1}, respectively. These results indicated that the introduction of the PDA layer would cover up the micro- and mesopores on the pristine fiber surface, while the growth of MoS_2 could effectively improve the specific surface area and pore volume of the final sample APM, rendering it with highly exposed active sites. Moreover, the lightweight APM with high porosity also exhibited excellent bendability, torsion ability and tensile resistance (Fig. 1(g)). These characteristics would undoubtedly endow the 3D co-catalyst with excellent comprehensive performance when used as a candidate material for the treatment of contaminated wastewater.

3.2. Performance of co-catalyst APM in removing BPA

The co-catalytic performance of APM was evaluated in the Fe^{2+}/PMS system for the degradation of typical organic pollutant BPA. Considering the vital role of synthetic conditions in the growth of MoS_2, the effect of reaction time on the performance of APM was

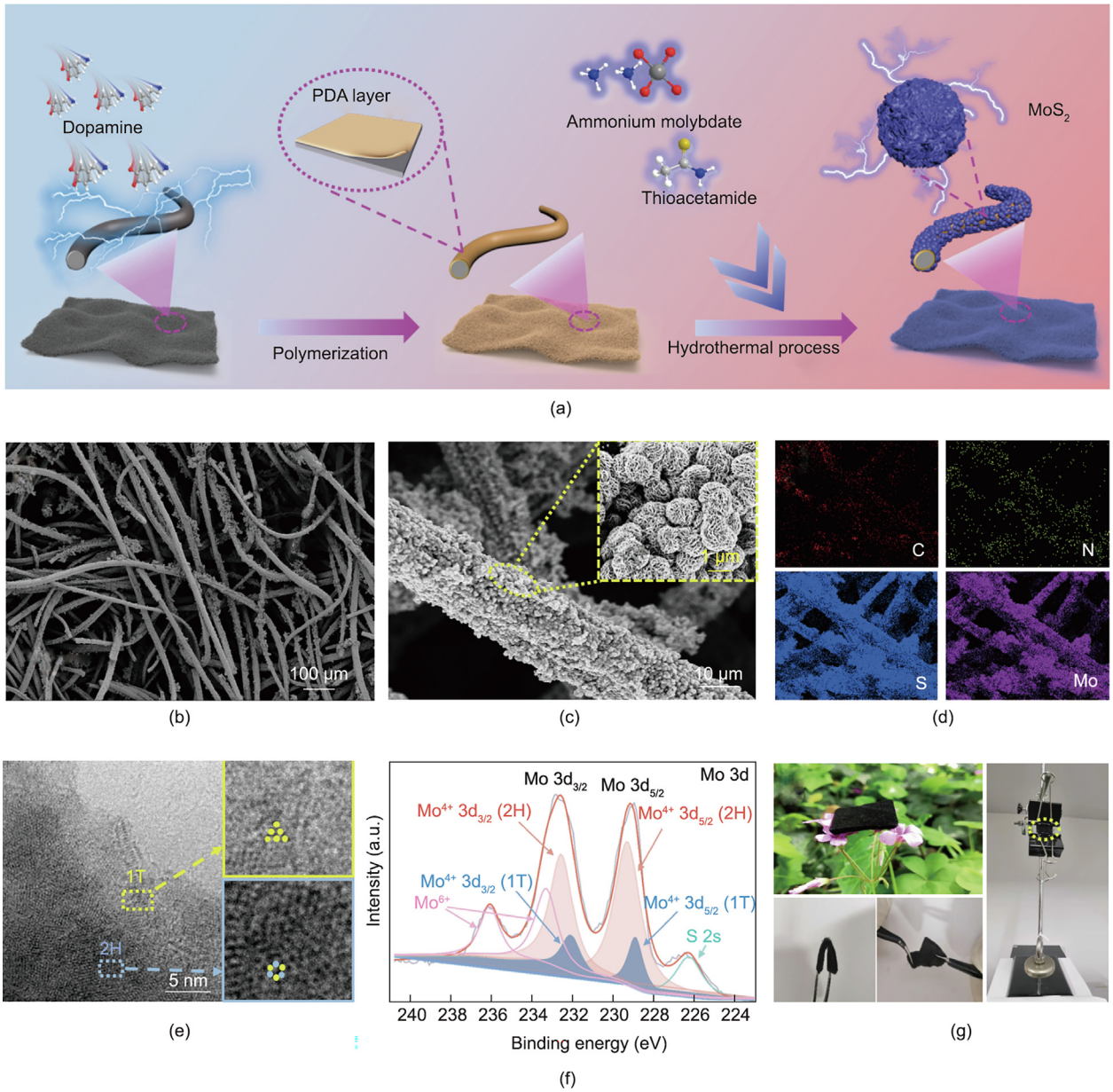

Fig. 1. (a) Schematic diagram for the preparation of APM. (b) and (c) SEM images of APM with different magnifications. (d) Corresponding element mappings of C, N, S, and Mo. (e) High-resolution transmission electron microscopy (HRTEM) image of APM. (f) XPS spectrum of Mo 3d for the synthesized APM. (g) Photographs of APM under different mechanical states.

first explored. As shown in Fig. 2(a), the APM–Fe^{2+}/PMS system exhibited the optimum catalytic ability for BPA removal when the hydrothermal treatment was lengthened to 18 h, therefore, this synthetic condition was selected for in-depth investigation. Fig. 2 (b) revealed the negligible adsorption of BPA on APM, and only 8.9% of BPA could be degraded in the presence of APM and PMS, indicating that APM itself could not directly trigger the decomposition of PMS. The homogenous Fe^{2+}/PMS system readily removed BPA at the initial stage, while the limited reduction rate of Fe^{3+} to Fe^{2+} inhibited the further activation of PMS, resulting in an inferior BPA removal rate of 48.2%. Moreover, neither the AP or AM showed obvious improvement in BPA degradation when coupled with the Fe^{2+}/PMS system, demonstrating that only the PDA layer or limited growth of MoS_2 on ACFs could barely regenerate the exhausted Fe^{2+} for continuous generation of ROS. Notably, when introducing the co-catalyst APM in the Fe^{2+}/PMS system, BPA could be promptly and completely degraded within 12 min. Meanwhile, the reaction rate (K_{obs}) of this system reached 0.455 min^{-1}, which was 2.5, 2.6, 2.8, and 65.0 times that of the AM–Fe^{2+}/PMS, AP–Fe^{2+}/PMS, Fe^{2+}/PMS and APM/PMS systems, respectively (Fig. 2(c)). These results suggested the critical roles of PDA and MoS_2 on APM, where the PDA layer on ACFs facilitated MoS_2 growth to assist Fe^{3+} reduction for enhanced PMS activation.

In general, the PMS activation process involves ROS generation, which can be identified using electron paramagnetic resonance (EPR) analysis and quenching experiments. As depicted in Fig. 2 (d), the paramagnetic signals of DMPO–·OH and DMPO–$SO_4^{\cdot-}$ adducts appeared in the Fe^{2+}/PMS system due to the heterolytic cleavage of PMS. The characteristic peak of DMPO–·OH was significantly intensified when APM was introduced into the Fe^{2+}/PMS system, indicating that the addition of co-catalyst APM could accelerate the production of ·OH. The variation of ROS in the

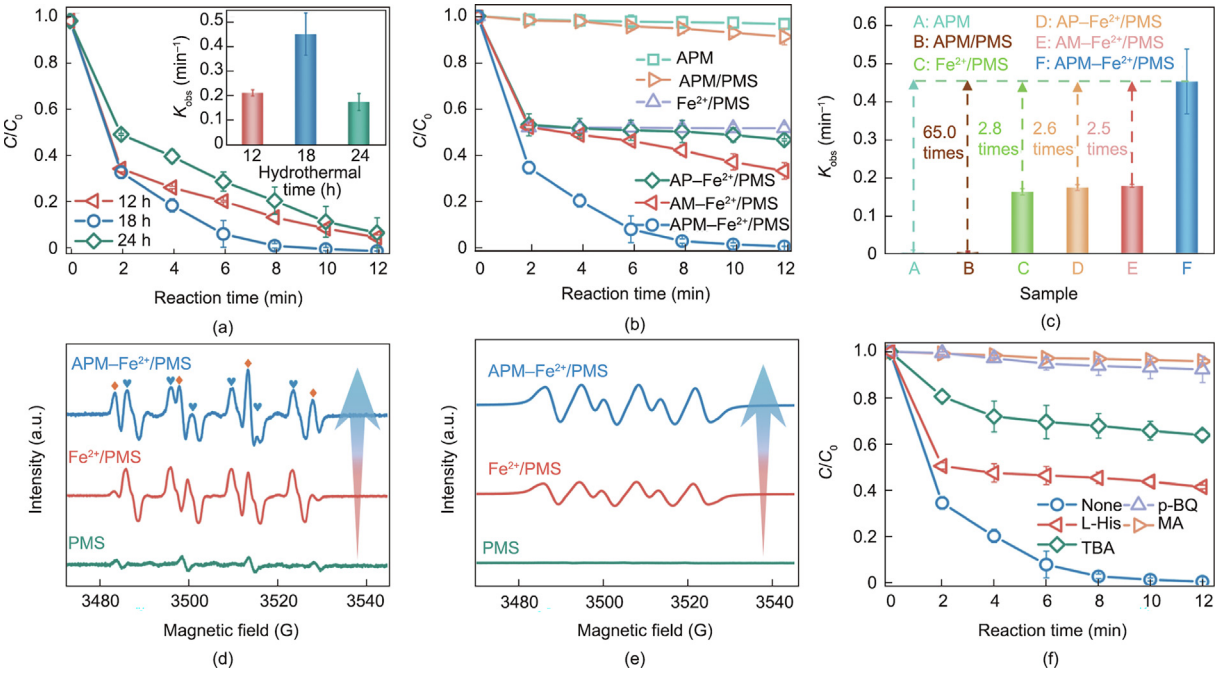

Fig. 2. (a) The BPA removal performance of APM synthesized with different hydrothermal times in co-catalytic system. (b) BPA removal under different systems and (c) their corresponding K_{obs} values. Electron paramagnetic resonance (EPR) spectra of (d) ·OH and $SO_4^{\cdot-}$ and (e) $O_2^{\cdot-}$ in the Fe^{2+}/PMS and APM–Fe^{2+}/PMS systems (DMPO–·OH: diamond symbol; DMPO–$SO_4^{\cdot-}$: heart symbol). (f) Effect of scavengers on BPA removal in APM–Fe^{2+}/PMS system. Conditions: C_{APM} = 0.50 g·L^{-1}, C_{Fe2+} = 0.04 × 10^{-3} mol·L^{-1}, C_{PMS} = 1.00 × 10^{-3} mol·L^{-1}, $C_{pollutants}$ = 50.00 × 10^{-6} mol·L^{-1}. *C*: concentration.

APM–Fe^{2+}/PMS system as the reaction progress was also recorded. The intensity of DMPO–·OH and DMPO-$SO_4^{\cdot-}$ adducts gradually decreased within 12 min (Fig. S10(a)), which signified that other active species might be present in the APM–Fe^{2+}/PMS system. Therefore, DMPO was used as the spin trapping agent to measure the formation of $O_2^{\cdot-}$ in MA solution. As shown in Fig. 2(e), the Fe^{2+}/PMS system could produce a certain amount of $O_2^{\cdot-}$, and the peak intensity of $O_2^{\cdot-}$ was further increased with the addition of APM. Moreover, the signal intensity of $O_2^{\cdot-}$ could be maintained at a high level throughout the reaction process (Fig. S10(b)), which meant that $O_2^{\cdot-}$ contributed greatly to the continuous removal of BPA. Further, the nitroblue tetrazolium (NBT) transformation experiments also supported the existence of $O_2^{\cdot-}$ in the APM–Fe^{2+}/PMS system (Fig. S11) [36]. In terms of $^1O_2$, no enhanced signal of TEMP-$^1O_2$ was observed in Fe^{2+}/PMS and APM–Fe^{2+}/PMS systems, and the peak intensity of TEMP-$^1O_2$ signal barely increased within 12 min (Fig. S12), indicating that $^1O_2$ was not involved in the degradation process. Similar results were also obtained by quenching tests. The removal rate of BPA was seriously inhibited when MA, TBA and p-BQ were added to the APM–Fe^{2+}/PMS system (Fig. 2(f)). The addition of excessive L-His also led to decreased BPA removal, which could be attributed to the consumption of PMS caused by the reaction between L-His and PMS, thus further affecting the generation of ROS in the system (Fig. S13) [37]. In addition, the high-valent iron species were generally formed in the Fe^{2+}/PMS system. To determine the role of high-valent iron species in the catalytic system, dimethyl sulfoxide (DMSO) was used as a trapping agent due to its specific oxygen-atom-transfer property. As shown in Fig. S14, even the concentration of DMSO reached up to 20 mmol·L^{-1}, the APM co-catalytic system still maintained a satisfactory removal efficiency, demonstrating the insignificant role of high-valent iron species in the degradation process. Combining the results above, it could be concluded that the APM–Fe^{2+}/PMS system mainly adopted ·OH, $SO_4^{\cdot-}$, and $O_2^{\cdot-}$ to eliminate BPA, and the addition of co-catalyst APM did not change the types of ROS in the system, but played a crucial role in promoting the generation of ROS.

To reveal the co-catalytic mechanism of APM, the variation of element valence and surface vacancy on APM were explored. The high-resolution Mo 3d spectrum demonstrated the increased content of Mo^{6+} on the APM surface after reaction (Fig. S15), confirming that Mo^{4+} was directly involved in the catalytic reaction and acted as the electron donor for Fe^{3+} reduction. After reaction, the concentration of leached Mo ions was 8.1 mg·L^{-1} by inductively coupled plasma optical emission spectrometer (ICP–OES) analysis, which was comparable with that in the previous MoS_2-based co-catalytic system [38]. Additionally, Fig. S16 demonstrated that several Fe peaks appeared on the APM after reaction, indicating that the electron transfer between the co-catalyst and Fe mainly occurred on the APM surface region. Moreover, the generation of S vacancies on the APM surface was specifically analyzed by the solid EPR spectrum. As expected, the paramagnetic signal corresponding to S vacancies was significantly intensified after reaction (Fig. S17), suggesting that the MoS_2 surface generated a large amount of S vacancies during the catalytic reaction and thus a large number of Mo^{4+} active sites were exposed on APM surface [39].

Based on the above experimental results and analysis, a reliable PMS activation mechanism integrating the APM co-catalytic effect on ROS generation was proposed. Specifically, Fe^{2+} generated a large amount of $SO_4^{\cdot-}$ by triggering PMS activation in the APM–Fe^{2+}/PMS system, accompanied by the conversion of Fe^{2+} to Fe^{3+} (Eq. (1)). Meanwhile, $SO_4^{\cdot-}$ in the system could react with H_2O to generate ·OH (Eq. (2)) [40], which further reacted with PMS to produce an abundance of $O_2^{\cdot-}$ (Eqs. (3) and (4)) [41]. In addition, a part of Fe^{2+} could also react with dissolved oxygen in the solution to form Fe^{3+} and $O_2^{\cdot-}$ (Eq. (5)), which was supported by the fact that the introduced N_2 inhibited BPA removal to a certain extent (Fig. S18) [42,43]. Subsequently, the generated Fe^{3+} could activate PMS for the dilatory generation of $O_2^{\cdot-}$ (Eq. (6)). Importantly, MoS_2 on the co-catalyst APM surface produced S vacancies by trapping

protons in the solution and exposed the active metal sites Mo^{4+} on the surface (Eq. (7)), thus facilitating the reduction of Fe^{3+} and ensuring the continuity of the entire catalytic reaction (Eq. (8)).

$$Fe^{2+} + HSO_5^- \rightarrow Fe^{3+} + SO_4^{\cdot-} + OH^- \quad (1)$$

$$SO_4^{\cdot-} + H_2O \rightarrow {}^{\cdot}OH + SO_4^{2-} + H^+ \quad (2)$$

$${}^{\cdot}OH + HSO_5^- \rightarrow SO_5^{\cdot-} + H_2O \quad (3)$$

$$SO_5^{\cdot-} + OH^- \rightarrow O_2^{\cdot-} + SO_4^{2-} + H^+ \quad (4)$$

$$Fe^{2+} + O_2 \rightarrow O_2^{\cdot-} + Fe^{3+} \quad (5)$$

$$Fe^{3+} + HSO_5^- + H_2O \rightarrow Fe^{2+} + O_2^{\cdot-} + 3H^+ + SO_4^{2-} \quad (6)$$

$$MoS_2 + 4H^+ \rightarrow 2H_2S + \equiv Mo^{4+} \quad (7)$$

$$\equiv Mo^{4+} + 2Fe^{3+} \rightarrow 2Fe^{2+} + \equiv Mo^{6+} \quad (8)$$

3.3. Comparation of APM–Fe^{2+}/PMS under batch-type and flow-through modes

In this study, the effect of experimental parameters on BPA degradation was investigated to optimize the reaction conditions. Besides the conventional parameters including the concentration of PMS and APM, reaction temperature, initial pH and aquatic environments (Figs. S19–S23), wastewater treatment volume which is an important component in realistic wastewater remediation but often overlooked in previous studies, was thoroughly explored in this study. In the traditional batch-type catalytic reaction, the K_{obs} of 50 mL BPA solution within 12 min was quite high (Fig. 3(a)). With further expansion of the solution volume, the K_{obs} and degradation rate gradually declined, and the final K_{obs} and degradation rate of the 100 mL BPA solution were only 0.172 min^{-1} and 86.0%, respectively (Fig. S24). A similar phenomenon was also identified when MoS_2 powder was used as the co-catalyst to treat the polluted solution with increased volume (Fig. S25). These results corroborated that traditional batch-type catalytic systems were incapable of dealing with a large volume of contaminated wastewater due to the poor diffusion rate of Fe species to the surface of co-catalysts. A flow-through co-catalytic system was specially designed to overcome the inherent drawback in batch-based mode (Figs. 3(b) and (c)), inspired by the membrane filtration process where the forced convection together with the confinement effect could synergistically enhance the mass transfer at the solution-membrane interface. Encouragingly, the BPA removal rate and K_{obs} of the APM–Fe^{2+}/PMS flow-through system could be maintained at a high level regardless of the pollutant solution volume (Fig. S26), and the system with the flow rates of 100–400 mL min^{-1} exhibited the similar degradation performance (Fig. S27). These results preliminarily indicated that the flow-through catalytic reaction had unexpected advantages in treating wastewater with expanded volume.

To better reveal the distinct performance of APM–Fe^{2+}/PMS in treating large volumes of polluted solution via batch-type and flow-through modes, the dynamic evolution of Fe^{2+} and Fe^{3+} concentrations during reaction were explored by using 1,10-phenanthrene and potassium thiocyanate (KSCN) as the complexes, respectively [44]. In the homogenous Fenton-like system (Fe^{2+}/PMS), 75.3% of Fe^{2+} was converted to Fe^{3+} in the first 4 min and remained at a low level during the following reaction due to the inherent rate-limiting step from Fe^{3+} to Fe^{2+} (Fig. S28). It was worth noting that when APM was added to the Fe^{2+}/PMS batch-type catalytic system, the Fe^{2+} concentration gradually increased at the early stage and slightly decreased after 16 min (Fig. 3(d)), but overall, the Fe^{2+} ratio in the APM batch-type catalytic system was much higher than that in the traditional Fe^{2+}/PMS system, which fully affirmed the co-catalytic ability of APM. Surprisingly, the Fe^{2+} concentration in the APM–Fe^{2+}/PMS flow-through catalytic system always maintained an upward trend, and the ratio of Fe^{2+} could finally reach an impressive value of 82.4% (Fig. 3(e)). To gain a more intuitive understanding of the co-catalytic performance in this work, we compared the Fe^{2+} regeneration properties of the APM–Fe^{2+}/PMS flow-through system with previously reported co-catalysts and found that the co-catalyst APM could regenerate a large amount of Fe^{2+} within only 16 min for equilibrium (Fig. 3(f) and Table S1) [13,24–26,30,45–49], which further consolidated the advancement of this reaction mode for Fe^{2+} recovery.

The consumption rate of PMS was calculated to compare the catalytic performance of Fe^{2+} in different reaction systems. Fig. S29 displayed that the Fe^{2+}/PMS catalytic system had the poor ability to activate PMS and only 7.3% of PMS was utilized after reaction. By contrast, the APM–Fe^{2+}/PMS batch-type and flow-through systems could continually consume PMS during the entire catalytic reaction process due to the sustainable Fe^{2+}/Fe^{3+} circulation assisted by the co-catalytic effect of APM (Fig. 3(g)). Additionally, the consumption rate of PMS in the APM–Fe^{2+}/PMS flow-through reaction was always higher than that in the batch-type system within 20 min, where only 3.9% of PMS remained in the flow-through system at the end of the reaction. Accordingly, the increased consumption of PMS was often accompanied by a higher content of ROS. Therefore, the amount of ROS produced in the APM–Fe^{2+}/PMS batch-type and flow-through modes was further explored by EPR analysis. As displayed in Fig. 3(h), the characteristic peak intensities of DMPO–${}^{\cdot}OH$ and DMPO–$SO_4^{\cdot-}$ in the APM–Fe^{2+}/PMS flow-through system were stronger than that in the batch-type system. Similarly, the signal peak of $O_2^{\cdot-}$ radical in the flow-through system also exhibited higher intensity (Fig. 3(i)). The increased ROS content in the solution could certainly contribute to the mineralization of organic pollutant. Fig. S30 illustrated that the APM–Fe^{2+}/PMS flow-through system could achieve 55.0% total organic carbon removal for BPA within 20 min, which was also superior to the batch-type catalysis. These results strongly suggested that the APM–Fe^{2+}/PMS flow-through system owned sufficient advantages over the batch-type mode in treating large volumes of pollutant wastewater.

To further illuminate the enhanced mass transfer effect induced by the flow-through mode, we employed CFDs simulations to visualize the velocity field in the 3D co-catalyst during the catalytic reaction. Considering that it was challenging to truly simulate the microfluidic flow inside the APM, we thus constructed five layers of interlaced fiber networks to represent the microchannels inside the substrate, and the fluid flow rate in the channels was visualized with warm and cold colors. As shown in Fig. 4(a), the fluid velocity in the flow-through mode ranged from 0.5 to 1.0 $m{\cdot}s^{-1}$, and this distribution of flow field enabled the optimal utilization of MoS_2 throughout the 3D substrate, which could greatly facilitate the intimate contact of reactants to maximally exploit the co-catalytic capacity of APM for Fe^{2+} regeneration. In contrast, the batch-type mode showed that almost no liquid flowed into the interior of APM due to the limited diffusive transport, implying that the reduction of Fe^{2+} mainly took place at the surface of the 3D bulk co-catalyst (Fig. 4(b)). To further consolidate the above results, we performed laser scanning confocal microscopy to monitor the reactant distribution under the flow-through and batch-type system. From the cross-sectional view of APM, we could clearly observe that the rhodamine B (RhB) in the flow-through system could enter the inside of the co-catalyst and be uniformly adsorbed by the whole APM, while the RhB was only

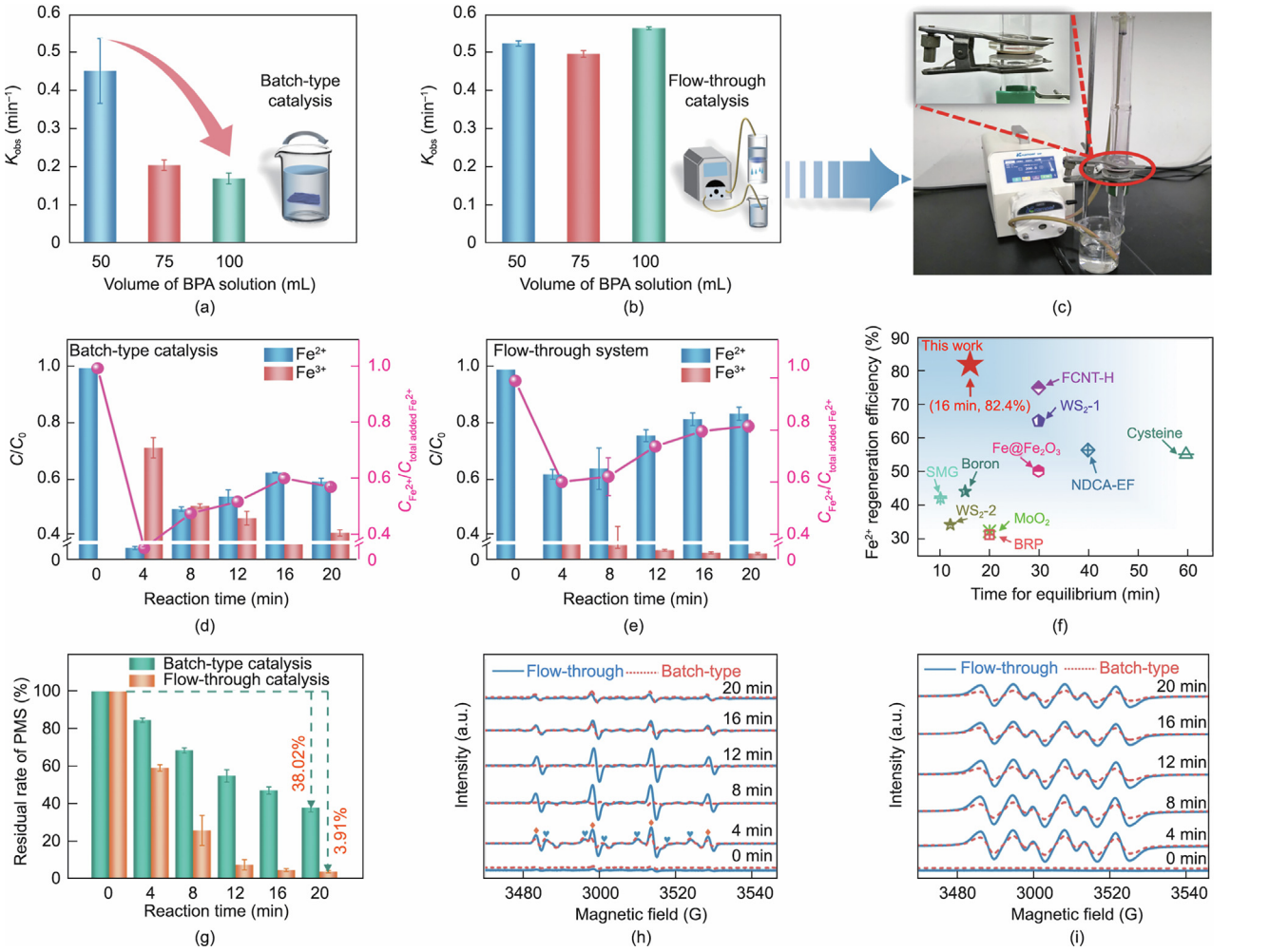

Fig. 3. The K_{obs} values of the APM–Fe^{2+}/PMS (a) batch-type and (b) flow-through reaction systems for BPA solution with different volumes. (c) Home-made flow-through catalytic reactor. Dynamic change of Fe^{2+} and Fe^{3+} concentrations in the APM–Fe^{2+}/PMS (d) batch-type and (e) flow-through reaction systems. (f) Comparation of Fe^{2+} regeneration efficiency in different co-catalyst systems. (g) Comparation of PMS decomposition rate in the APM–Fe^{2+}/PMS batch-type and flow-through systems. EPR spectra of (h) ·OH and $SO_4^{\cdot-}$ and (i) $O_2^{\cdot-}$ adducts in the APM–Fe^{2+}/PMS batch-type and flow-through systems. Conditions: m_{APM} = 0.25 g, C_{Fe2+} = 0.04 × 10^{-3} mol·L^{-1}, C_{PMS} = 1.00 × 10^{-3} mol·L^{-1}, $C_{pollutants}$ = 50.00 × 10^{-6} mol·L^{-1}. *m*: mass.

distributed on the surface part of APM in the batch-type system (Figs. 4(c) and (d)).

Since the geometry of the flow channel had a certain influence on the behavior of the fluid [50], we also investigated the effect of fiber morphology on the velocity field. Fig. 4(e) illustrated that the flower globose-like MoS_2 particles on the fiber surface could induce the rotation of flow lines and reduce the thickness of the boundary layer in the vicinity of fiber surface, thus favoring the reactant mixing and mass transfer [51]. In contrast, no local turbulence was observed near the smooth surface of pristine ACFs (Fig. 4(f)), which demonstrated that the MoS_2 particles played a significant role in enhancing the transfer of electrons and reactants at the interfacial region of APM. These findings provided further evidence for the excellent oxidation capacity in the flow-through reaction system.

3.4. Applications of flow-through catalytic system in wastewater purification

The universal capability of the APM–Fe^{2+}/PMS flow-through system for remediation of the emerging pollutants was explored in this study. The co-catalytic system possessed excellent degradation activity to a broad spectrum of organic pollutants with diverse molecular structures, including pharmaceuticals (carbamazepine (CBZ), atrazine (ATZ) and diclofenac (DCF)), phenolic compounds (phenol, 4-chlorophenol (4-CP) and p-nitrophenol (P-NP)) and organic dyes (acid red 1 (AR1), RhB and reactive red 195 (3BF), Fig. 5(a)). Moreover, we collected tap water and lake water to investigate the adaptability of the constructed system in complex environments. Encouragingly, after treatment for just 12 min via the APM–Fe^{2+}/PMS flow-through system, the removal rates of BPA in the two kinds of water quality were still as high as 91.5% and 88.2%, respectively (Fig. 5(b)). In addition, the recycling performance of co-catalyst APM in the bath-type and flow-through mode was also investigated. As illustrated in Fig. 5(c), the flow-through system could still remove 85.2% of BPA after repeated use for 20 times, far outperforming other co-catalysts in AOPs (Table S2) [30,42,45,52–55]. In contrast, the catalytic performance dramatically declined in bath-type mode with increased repeating cycles, which strongly demonstrated the advancement of the flow-through system in full utilization of active sites inside the 3D co-catalyst. To highlight the feasibility of the APM flow-through system in treating large amounts of wastewater, we scaled up the testing system from 100 mL to 1 L and compared the performance with other synthetic or purchased co-catalysts coupled with bath-type Fe^{2+}/PMS system. As shown in Fig. 5(d), the metal-free

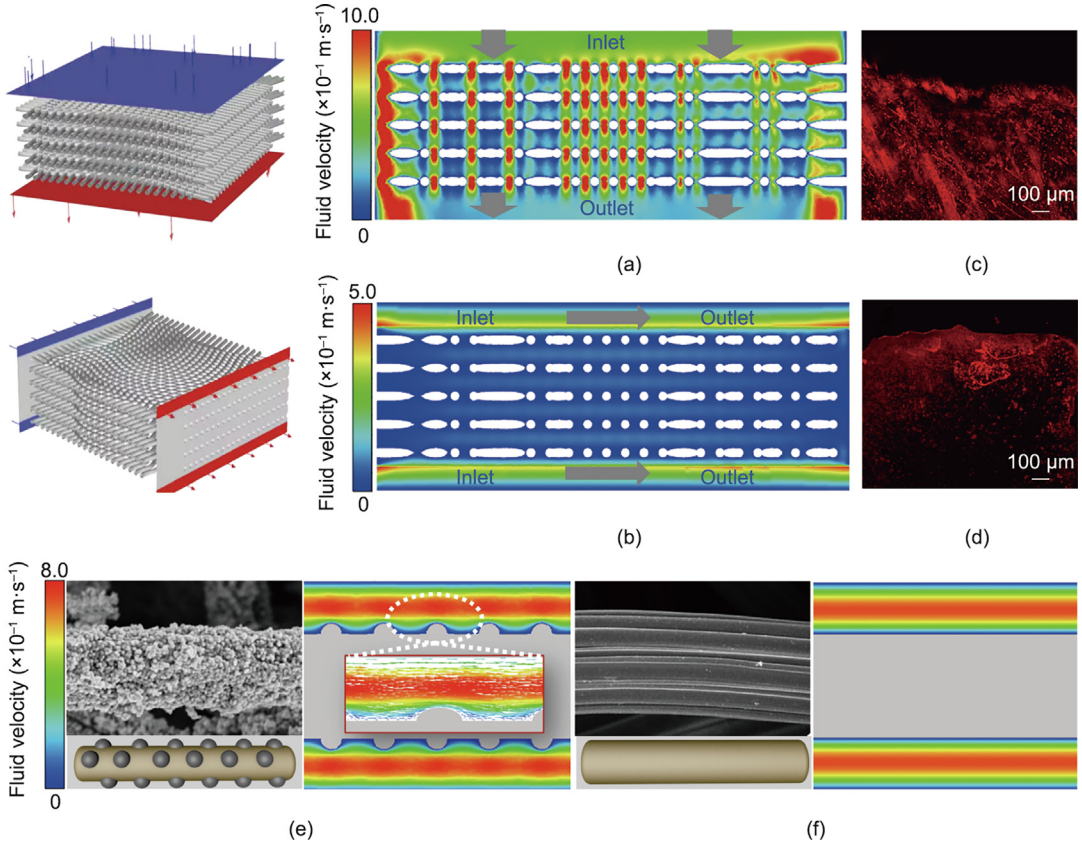

Fig. 4. Views of the flow behaviors in the (a) flow-through and (b) batch-type systems obtained from CFD calculations. The laser scanning confocal microscopy images of the cross-sectional view of the APM after rhodamine B (RhB) adsorption under the (c) flow-through and (d) batch-type mode. The velocity vector field in the microchannels of the (e) MoS_2 modified and (f) pristine carbon fibers.

co-catalysts including boron, phosphorus and carbon usually had low toxicity and appropriate electron activity for Fe^{3+} reduction [15], but their co-catalytic systems could only remove less than 30% of pollutants. As for the metal oxides, although the reducing metal sites could accelerate the Fe^{3+}/Fe^{2+} conversion to some extent, the removal rate of BPA was still unsatisfactory (13.1%–79.4%). In addition, metal sulfides generally possessed superior physical and chemical properties such as higher electrical conductivity and increased reducing species than those of the corresponding oxides [56], thus exhibiting more excellent performance in Fe^{2+} regeneration. However, the reduction capability of metal sulfides in powder state was still inferior due to the mass transfer limitation in treating large volume of wastewater. Comparably, the APM flow-through system could remove BPA up to 98.7% in 60 min, which was much higher than that of the previously reported co-catalysts, further confirming the superiority of the co-catalyst APM combined with the flow-through mode.

It is noteworthy that the discharge of sewage in the industrial production process often contains not only organic pollutants, but also oily compounds that are difficult to handle, which may have nonnegligible impacts on the treatment of polluted water [57]. Therefore, it was crucial to explore the effect of oil pollution on the surface properties and the subsequent degradation capability of the catalytic materials. To this end, the oil pollution resistance of the prepared samples was first investigated, where the different underwater states of oil droplet adhesion and oil contact angle (OCA) on the material surface were recorded. For the ACFs and AP, an obvious droplet deformation was observed when an oil droplet was forced to sufficiently contact the material surface and then lift up (Fig. 6(a)), indicating the undesired oil adhesion on the material surface. In contrast, the oil droplet on the APM surface did not produce obvious deformation and left the surface smoothly in the slow pulling upward process, suggesting the excellent underwater superoleophobic property of APM. The underwater OCA test also supported this result. By growing the MoS_2 particles on the carbon fiber surface, the underwater OCA of APM increased to 154° (Fig. 6(b)). The enhanced underwater oil-repellent ability of the APM could be attributed to the improved hydrophilicity and surface roughness endowed by the MoS_2 particles, which could trap water into the porous structure and form a stable hydration layer, thus circumventing the direct contact between oil droplets and material surface [58]. Moreover, the stability of the oil-repellent property of APM in various aqueous environments (e.g., acid, alkaline, and salt solutions) was also evaluated. When the APM was immersed in the 1 $mol \cdot L^{-1}$ target solutions for 3 h, the underwater OCA hardly changed (decreased only by 8°, 4°, and 9°, Fig. 6(c)), which further confirmed the marvelous durability of APM surface structure under extreme water environment.

Considering the opposite wettability towards oil and water, the prepared superhydrophilic APM could be applied to oil/water separation. Thus, four oil/water mixtures, including surfactant-free, nonionic (Tween-80), cationic (cetyltrimethyl ammonium bromide (CTAB)) and anionic (sodium dodecyl sulfate (SDS)) surfactant-stabilized oil/water emulsions, were prepared to evaluate the separation efficiency of the APM. As illustrated in Fig. 6(d), the removal rates of four target emulsions by APM flow-through system within 12 min were 76.3%, 97.5%, 95.1%, and 95.8%, respectively. Similarly, the optical photos showed that these oil/water emulsions changed from red to transparent in color after

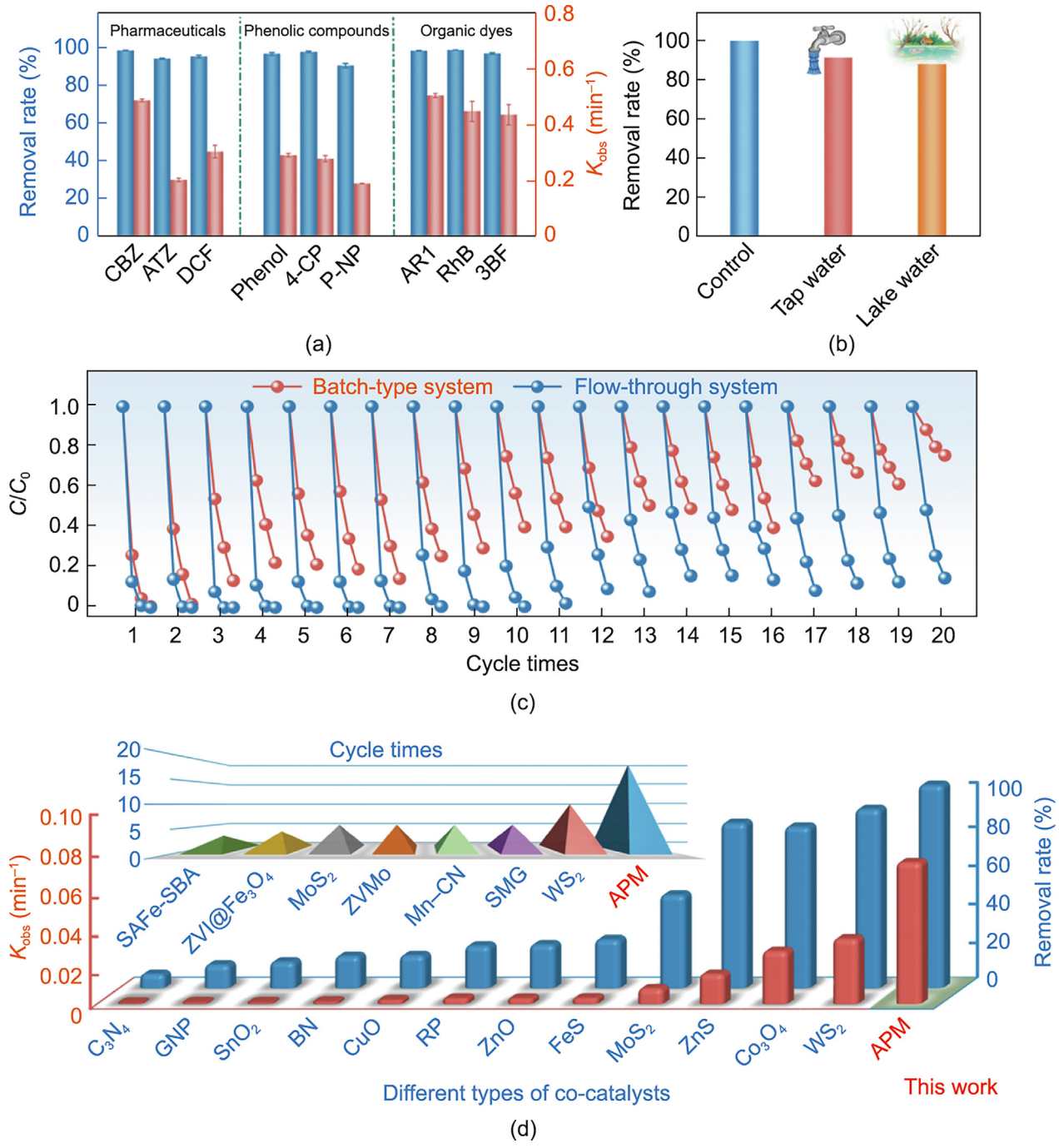

Fig. 5. (a) The degradation performance of APM–Fe^{2+}/PMS flow-through system for different organic pollutants. (b) Different water environments on BPA removal of APM–Fe^{2+}/PMS flow-through system. (c) Cyclic performance of co-catalyst APM under flow-through and batch-type modes. (d) Comparation of APM–Fe^{2+}/PMS flow-through system with other metal sulfides, metal oxides and nonmetallic elements coupled with bath-type Fe^{2+}/PMS system. Conditions: m_{APM} = 0.25 g, C_{Fe2+} = 0.04 × 10^{-3} mol·L^{-1}, C_{PMS} = 1.00 × 10^{-3} mol·L^{-1}, $C_{pollutants}$ = 50.00 × 10^{-6} mol·L^{-1}.

separation, implying that most of the oil droplets in the water were successfully removed. To further consolidate the effectiveness of the APM–Fe^{2+}/PMS flow-through system in treating the sewage with intricate components, BPA was added into the above four different oil/water emulsions to simulate complex oily wastewater. As displayed in Fig. 6(e), in the stable oil/water emulsions of Tween 80, the BPA removal rate of APM–Fe^{2+}/PMS flow-through system was as high as 94.0% within 12 min, which was much better than the 45.1% BPA removal rate of batch-type mode. Similar results were also observed for the flow-through system in treating other types of oily wastewater, where over 91.9%, 94.9%, and 96.4% BPA removal rates could be achieved. This interesting phenomenon might be attributed to the fact that in the traditional batch-type catalytic reaction, the oil droplets in oily wastewater would attach to the APM surface and retard the intimate interaction between Fe ions and MoS_2 on the APM. Moreover, the limited diffusive transport in the batch-type mode hindered the effective utilization of active sites inside the 3D co-catalyst, thus causing the rapid decline of BPA removal rate in oily wastewater. While in the flow-through system, the emulsified oil droplets could initially be separated and then the Fe^{3+} permeated into the APM to start the regeneration process. This alleviated the negative impact of oil droplets on

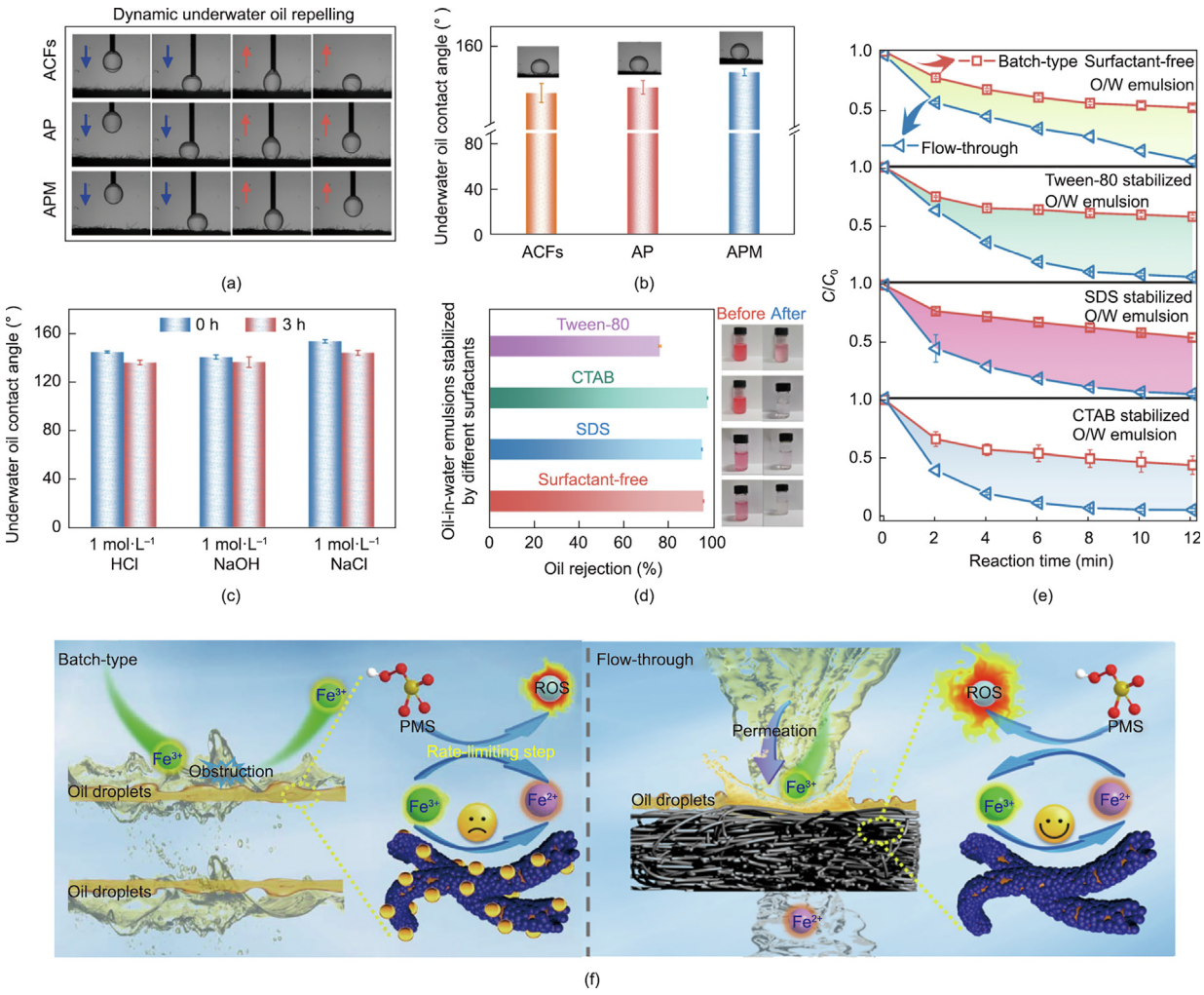

Fig. 6. (a) Adhesion states of underwater oil droplet on ACFs, AP, and APM surfaces. (b) Variation of underwater OCA of the prepared samples. (c) The change of underwater OCA of APM after immersing in acid, alkali and salt solutions for 3 h. (d) The separation efficiency of APM for different types of oil/water mixtures. (e) The BPA removal rate in the oily wastewater by using APM under flow-through and batch-type modes. (f) Reaction mechanism of treating oily wastewater with batch-type and flow-through systems. Conditions: m_{APM} = 0.25 g, C_{Fe2+} = 0.04 × 10^{-3} mol·L^{-1}, C_{PMS} = 1.00 × 10^{-3} mol·L^{-1}, $C_{pollutants}$ = 50.00 × 10^{-6} mol·L^{-1}.

catalytic degradation (Fig. 6(f)). In short, the excellent co-catalytic capability, improved mass transfer and strong adaptability exhibited in complex wastewater environments consolidated the outstanding application potential of the flow-through catalytic system presented in this study.

4. Conclusion

In this study, we present an innovative flow-through design to address the two fundamental challenges in co-catalytic AOPs reactions: the tedious procedure in co-catalyst recovery and the limited mass transfer in catalytic reaction. Compared with the traditional powder co-catalyst and the batch-type reaction mode, the advantages of the APM–Fe^{2+}/PMS flow-through system can be summarized as follows: ① the uniform growth of MoS_2 on the robust macroscopic ACFs bypass the redundancy of co-catalyst recovery and maintain its excellent co-catalytic capacity for more than 20 cycles; ② the convection-enhanced mass transfer in flow-through mode achieves the full utilization of active sites inside the 3D co-catalyst and accelerates the Fe^{3+}/Fe^{2+} circulation (equilibrium Fe^{2+} ratio of 82.4%) for efficient ROS production; ③ the APM with superwetting property can also tackle the intricate oily wastewater without loss of pollutant degradation efficiency through pre-interception of oil droplets. We believe that the outstanding comprehensive performance achieved in this ingeniously designed flow-through co-catalyst system can build a reliable platform for practical environmental remediation.

Compliance with ethics guidelines

Weiyang Lv, Hao Li, Jinhui Wang, Lixin Wang, Zenglong Wu, Yuge Wang, Wenkai Song, Wenkai Cheng, and Yuyuan Yao declare that they have no conflict of interest.

Acknowledgments

This work was supported by the National Natural Science Foundation of China (52003240), Zhejiang Provincial Natural Science Foundation of China (LQ21B070007) and China Postdoctoral Science Foundation (2022M722818).

Appendix A. Supplementary material

Supplementary data to this article can be found online at https://doi.org/10.1016/j.eng.2023.06.010.

References

[1] Tang Z, Liu Y, He M, Bu W. Chemodynamic therapy: tumour microenvironment-mediated Fenton and Fenton-like reactions. Angew Chem Int Ed Engl 2019;58(4):946–56.
[2] Jin S, Shao W, Luo X, Wang H, Sun X, He X, et al. Spatial band separation in a surface doped heterolayered structure for realizing efficient singlet oxygen generation. Adv Mater 2022;34(47):e2206516.
[3] Giannakis S, Lin KYA, Ghanbari F. A review of the recent advances on the treatment of industrial wastewaters by sulfate radical-based advanced oxidation processes (SR-AOPs). Chem Eng J 2021;406:127083.
[4] Wang J, Li B, Li Y, Fan X, Zhang F, Zhang G, et al. Facile synthesis of atomic Fe–N–C materials and dual roles investigation of Fe-N_4 sites in Fenton-like reactions. Adv Sci (Weinh) 2021;8(22):e2101824.
[5] Song N, Ren S, Zhang Y, Wang C, Lu X. Confinement of prussian blue analogs boxes inside conducting polymer nanotubes enables significantly enhanced catalytic performance for water treatment. Adv Funct Mater 2022;32(34):2204751.
[6] Ding D, Mei Z, Huang H, Feng W, Chen L, Chen Y, et al. Oxygen-independent sulfate radical for stimuli-responsive tumor nanotherapy. Adv Sci (Weinh) 2022;9(17):e2200974.
[7] Li J, Li M, Sun H, Ao Z, Wang S, Liu S. Understanding of the oxidation behavior of benzyl alcohol by peroxymonosulfate via carbon nanotubes activation. ACS Catal 2020;10(6):3516–25.
[8] Zhang LS, Jiang XH, Zhong ZA, Tian L, Sun Q, Cui YT, et al. Carbon nitride supported high-loading Fe single-atom catalyst for activation of peroxymonosulfate to generate $^1O_2$ with 100% selectivity. Angew Chem Int Ed Engl 2021;60(40):21751–5.
[9] Gao Y, Rao Y, Ning H, Chen J, Zeng Q, Tian F, et al. Comparative investigation of diclofenac degradation by Fe^{2+}/chlorine and Fe^{2+}/PMS processes. Separ Purif Tech 2022;297:121555.
[10] Bao Y, Lian C, Huang K, Yu H, Liu W, Zhang J, et al. Generating high-valent iron-oxo equivalent to Fe-IV=O complexes in neutral microenvironments through peroxymonosulfate activation by Zn-Fe layered double hydroxides. Angew Chem Int Ed Engl 2022;61:202209542.
[11] Sheng B, Zhou X, Shi Z, Wang Z, Guo Y, Lou X, et al. Is addition of reductive metals (Mo, W) a panacea for accelerating transition metals-mediated peroxymonosulfate activation? J Hazard Mater 2020;386:121877.
[12] Tian Y, Wu Y, Yi Q, Zhou L, Lei J, Wang L, et al. Singlet oxygen mediated Fe^{2+}/peroxymonosulfate photo-Fenton-like reaction driven by inverse opal WO_3 with enhanced photogenerated charges. Chem Eng J 2021;425:128644.
[13] Liu M, Feng Z, Luan X, Chu W, Zhao H, Zhao G. Accelerated Fe^{2+} regeneration in an effective electro-Fenton process by boosting internal electron transfer to a nitrogen-conjugated Fe(III) complex. Environ Sci Tech 2021;55(9):6042–51.
[14] Song G, Du X, Zheng Y, Su P, Tang Y, Zhou M. A novel electro-Fenton process coupled with sulfite: enhanced Fe^{3+} reduction and TOC removal. J Hazard Mater 2022;422:126888.
[15] Zhou H, Zhang H, He Y, Huang B, Zhou C, Yao G, et al. Critical review of reductant-enhanced peroxide activation processes: trade-off between accelerated Fe^{3+}/Fe^{2+} cycle and quenching reactions. Appl Catal B 2021;286:119900.
[16] Zhu Y, Zhu R, Xi Y, Zhu J, Zhu G, He H. Strategies for enhancing the heterogeneous Fenton catalytic reactivity: a review. Appl Catal B 2019;255:117739.
[17] Lin J, Tian W, Guan Z, Zhang H, Duan X, Wang H, et al. Functional carbon nitride materials in photo-Fenton-like catalysis for environmental remediation. Adv Funct Mater 2022;32(24):2201743.
[18] Yan Q, Zhang J, Xing M. Cocatalytic Fenton reaction for pollutant control. Cell Rep Phys Sci 2020;1(8):100149.
[19] Zhou H, Peng J, Duan X, Yin H, Huang B, Zhou C, et al. Redox-active polymers as robust electron-shuttle Co-catalysts for fast Fe^{3+}/Fe^{2+} circulation and green Fenton oxidation. Environ Sci Tech 2023;57(8):3334–44.
[20] Hou X, Zhan G, Huang X, Wang N, Ai Z, Zhang L. Persulfate activation induced by ascorbic acid for efficient organic pollutants oxidation. Chem Eng J 2020;382:122355.
[21] Shi X, Li Y, Zhang Z, Sun L, Peng Y. Enhancement of ciprofloxacin degradation in the Fe(II)/peroxymonosulfate system by protocatechuic acid over a wide initial pH range. Chem Eng J 2019;372:1113–21.
[22] Sang W, Li Z, Huang M, Wu X, Li D, Mei L, et al. Enhanced transition metal oxide based peroxymonosulfate activation by hydroxylamine for the degradation of sulfamethoxazole. Chem Eng J 2020;383:123057.
[23] Zhou C, Zhou P, Sun M, Liu Y, Zhang H, Xiong Z, et al. Nitrogen-doped carbon nanotubes enhanced Fenton chemistry: role of near-free iron(III) for sustainable iron(III)/iron(II) cycles. Water Res 2022;210:117984.
[24] Zhou H, Peng J, Li J, You J, Lai L, Liu R, et al. Metal-free black-red phosphorus as an efficient heterogeneous reductant to boost Fe^{3+}/Fe^{2+} cycle for peroxymonosulfate activation. Water Res 2021;188:116529.
[25] Zhou P, Ren W, Nie G, Li X, Duan X, Zhang Y, et al. Fast and long-lasting iron(III) reduction by boron toward green and accelerated Fenton chemistry. Angew Chem Int Ed Engl 2020;59(38):16517–26.
[26] Ji J, Aleisa RM, Duan H, Zhang J, Yin Y, Xing M. Metallic active sites on MoO2 (110) surface to catalyze advanced oxidation processes for efficient pollutant removal. iScience 2020;23(2):100861.
[27] Yan Q, Lian C, Huang K, Liang L, Yu H, Yin P, et al. Constructing an acidic microenvironment by MoS_2 in heterogeneous Fenton reaction for pollutant control. Angew Chem Int Ed Engl 2021;60(31):17155–63.
[28] Liu W, Fu P, Zhang Y, Xu H, Wang H, Xing M. Efficient hydrogen production from wastewater remediation by piezoelectricity coupling advanced oxidation processes. Proc Natl Acad Sci USA 2023;120(7):e2218813120.
[29] Jiang L, Wei Z, Ding Y, Ma Y, Fu X, Sun J, et al. In-situ synthesis of self-standing cobalt-doped nickel sulfide nanoarray as a recyclable and integrated catalyst for peroxymonosulfate activation. Appl Catal B 2022;307:121184.
[30] Zhu L, Ji J, Liu J, Mine S, Matsuoka M, Zhang J, et al. Designing 3D-MoS_2 sponge as excellent cocatalysts in advanced oxidation processes for pollutant control. Angew Chem Int Ed Engl 2020;59(33):13968–76.
[31] Liu Y, Qu R, Li X, Zhai H, Zhao S, Wei Y, et al. Integration of catalytic capability and pH-responsive wettability in a VxOy-based dual-mesh system: towards solving the trade-off between the separation flow rate and degradation efficiency. J Mater Chem A Mater Energy Sustain 2021;9(9):5454–67.
[32] Qiao W, Xu W, Xu X, Wu L, Yan S, Wang D. Construction of active orbital via single-atom cobalt anchoring on the surface of 1T-MoS_2 basal plane toward efficient hydrogen evolution. ACS Appl Energy Mater 2020;3(3):2315–22.
[33] Liu Y, Ai K, Lu L. Polydopamine and its derivative materials: synthesis and promising applications in energy, environmental, and biomedical fields. Chem Rev 2014;114(9):5057–115.
[34] Goloveshkin AS, Lenenko ND, Naumkin AV, Pereyaslavtsev AY, Grigorieva AV, Shapovalov AV, et al. Enhancement of 1T-MoS_2 superambient temperature stability and hydrogen evolution performance by intercalating a phenanthroline monolayer. ChemNanoMat 2021;7(4):447–56.
[35] Liu Y, Li Y, Peng F, Lin Y, Yang S, Zhang S, et al. 2H- and 1T- mixed phase few-layer MoS_2 as a superior to Pt co-catalyst coated on TiO_2 nanorod arrays for photocatalytic hydrogen evolution. Appl Catal B 2019;241:236–45.
[36] Jiang XH, Xing QJ, Luo XB, Li F, Zou JP, Liu SS, et al. Simultaneous photoreduction of Uranium(VI) and photooxidation of Arsenic(III) in aqueous solution over g-C_3N_4/TiO_2 heterostructured catalysts under simulated sunlight irradiation. Appl Catal B 2018;228:29–38.
[37] Yun ET, Lee JH, Kim J, Park HD, Lee J. Identifying the nonradical mechanism in the peroxymonosulfate activation process: singlet oxygenation versus mediated electron transfer. Environ Sci Tech 2018;52(12):7032–42.
[38] Kuang H, He Z, Li M, Huang R, Zhang Y, Xu X, et al. Enhancing co-catalysis of MoS_2 for persulfate activation in Fe^{3+}-based advanced oxidation processes via defect engineering. Chem Eng J 2021;417:127987.
[39] Huang Y, Lai L, Huang W, Zhou H, Li J, Liu C, et al. Effective peroxymonosulfate activation by natural molybdenite for enhanced atrazine degradation: role of sulfur vacancy, degradation pathways and mechanism. J Hazard Mater 2022;435:128899.
[40] Chen C, Feng H, Deng Y. Re-evaluation of sulfate radical based-advanced oxidation processes (SR-AOPs) for treatment of raw municipal landfill leachate. Water Res 2019;153:100–7.
[41] Wang J, Duan H, Wang M, Shentu Q, Xu C, Yang Y, et al. Construction of durable superhydrophilic activated carbon fibers based material for highly-efficient oil/water separation and aqueous contaminants degradation. Environ Res 2022;207:112212.
[42] Yi Q, Ji J, Shen B, Dong C, Liu J, Zhang J, et al. Singlet oxygen triggered by superoxide radicals in a molybdenum cocatalytic Fenton reaction with enhanced REDOX activity in the environment. Environ Sci Tech 2019;53(16):9725–33.
[43] Zhang C, Kong C, Tratnyek PG, Qin C. Generation of reactive oxygen species and degradation of pollutants in the Fe^{2+}/O_2/tripolyphosphate system: regulated by the concentration ratio of Fe^{2+} and tripolyphosphate. Environ Sci Tech 2022;56(7):4367–76.
[44] Xu L, Qi L, Han Y, Lu W, Han J, Qiao W, et al. Improvement of Fe^{2+}/peroxymonosulfate oxidation of organic pollutants by promoting Fe^{2+} regeneration with visible light driven g-C_3N_4 photocatalysis. Chem Eng J 2022;430:132828.
[45] Xiao Y, Ji J, Zhu L, Bao Y, Liu X, Zhang J, et al. Regeneration of zero-valent iron powder by the cocatalytic effect of WS_2 in the environmental applications. Chem Eng J 2020;383:123158.
[46] Shi J, Ai Z, Zhang L. Fe@Fe_2O_3 core-shell nanowires enhanced Fenton oxidation by accelerating the Fe(III)/Fe(II) cycles. Water Res 2014;59:145–53.
[47] Yang Z, Yu A, Shan C, Gao G, Pan B. Enhanced Fe(III)-mediated Fenton oxidation of atrazine in the presence of functionalized multi-walled carbon nanotubes. Water Res 2018;137:37–46.
[48] Dong C, Ji J, Shen B, Xing M, Zhang J. Enhancement of H_2O_2 decomposition by the co-catalytic effect of WS_2 on the Fenton reaction for the synchronous reduction of Cr(VI) and remediation of phenol. Environ Sci Tech 2018;52(19):11297–308.
[49] Li T, Zhao Z, Wang Q, Xie P, Ma J. Strongly enhanced Fenton degradation of organic pollutants by cysteine: an aliphatic amino acid accelerator outweighs hydroquinone analogues. Water Res 2016;105:479–86.
[50] Song R, Chi H, Ma Q, Li D, Wang X, Gao W, et al. Highly efficient degradation of persistent pollutants with 3D nanocone TiO_2-based photoelectrocatalysis. J Am Chem Soc 2021;143(34):13664–74.
[51] Pérez JF, Llanos J, Sáez C, López C, Cañizares P, Rodrigo MA. Development of an innovative approach for low-impact wastewater treatment: a microfluidic flow-through electrochemical reactor. Chem Eng J 2018;351:766–72.
[52] Sheng B, Yang F, Wang Y, Wang Z, Li Q, Guo Y, et al. Pivotal roles of MoS_2 in boosting catalytic degradation of aqueous organic pollutants by Fe(II)/PMS. Chem Eng J 2019;375:121989.
[53] Xia Q, Yao Z, Zhang D, Li D, Zhang Z, Jiang Z. Rational synthesis of micronano dendritic ZVI@Fe_3O_4 modified with carbon quantum dots and oxygen

vacancies for accelerating Fenton-like oxidation. Sci Total Environ 2019;671:1056–65.
[54] Guo Z, Xie Y, Xiao J, Zhao ZJ, Wang Y, Xu Z, et al. Single-atom Mn-N_4 site-catalyzed peroxone reaction for the efficient production of hydroxyl radicals in an acidic solution. J Am Chem Soc 2019;141(30):12005–10.
[55] Yin Y, Shi L, Li W, Li X, Wu H, Ao Z, et al. Boosting Fenton-like reactions via single atom Fe catalysis. Environ Sci Tech 2019;53(19):11391–400.
[56] Huang M, Wang X, Liu C, Fang G, Gao J, Wang Y, et al. Mechanism of metal sulfides accelerating Fe(II)/Fe(III) redox cycling to enhance pollutant degradation by persulfate: metallic active sites vs. reducing sulfur species. J Hazard Mater 2021;404(Pt B):124175.
[57] You X, Wang M, Jiang G, Zhao X, Wang Z, Liu F, et al. Multifunctional porous nanofibrous membranes with superior antifouling properties for oil-water separation and photocatalytic degradation. J Membr Sci 2023;668:121245.
[58] Meng X, Wang M, Heng L, Jiang L. Underwater mechanically robust oil-repellent materials: combining conflicting properties using a heterostructure. Adv Mater 2018;30:1706634.